Physica Medica 64 (2019) 33–39

Contents lists available at ScienceDirect

Physica Medica

journal homepage: www.elsevier.com/locate/ejmp

Technical note

Estimation of respiratory phases during proton radiotherapy from a 4D-CT and Prompt gamma detection profiles

Jaroslav Albert[a,*], Rudi Labarbe[b], Guillaume Janssens[b], Kevin Souris[a,c], Edmond Sterpin[c,d]

[a] Université Catholique de Louvain, Institute of Information and Communication Technologies, Electronics and Applied Mathematics, Louvain-la-Neuve, Belgium
[b] Ion Beam Application SA, Louvain-la-Neuve, Belgium
[c] Université Catholique de Louvain, Molecular Imaging Radiotherapy and Oncology, Brussels, Belgium
[d] KU Leuven, Department of Oncology, Laboratory of Experimental Radiotherapy, Leuven, Belgium

ARTICLE INFO

Keywords:
Proton radiotherapy
Prompt gamma camera
Lung cancer
Respiratory phases
4D-CT
Internal surrogate

ABSTRACT

Proton radiotherapy has a potential to provide an effective cancer treatment while sparing greater volume of healthy tissue than the conventional X-ray based radiotherapy. However, in lungs this potential is hindered by motion due to breathing. An important quantity in treatment verification is the correlation between the respiratory phases (RP) and the timing of pencil beam scanning (PBS). In this note, we demonstrate how the RP can be estimated using Prompt gamma (PG) detection profiles collected during a treatment. We utilized a 4D-CT of a patient with lung cancer, a treatment plan and a PG simulator. The treatment plan consisted of ten layers corresponding to ten proton energies. The RPs of the 4D-CT were interpolated using a deformable registration algorithm, so as to have fifty RPs in total. Deviations from regular breathing were introduced via time dependent frequency modulation. Fifty unique breathing patterns were generated, for which PG profiles were simulated for each pencil beam. Poisson noise was added to each PG profile to account for photon statistics. The RPs were estimated by comparing the PG profiles with and without Poisson noise via three different methods: the RP associated with each layer was estimated 1) independently of the other layers, 2) using a linear correlation between the layers, and 3) using a quadratic correlation between the layers. The best model, the quadratic model, yielded an average error in RP estimation relative to the breathing period of 5% of the breathing period or less with a 90% confidence interval.

1. Introduction

Proton radiotherapy can offer better sparing of healthy tissue than a conventional X-ray based therapy. However, a major drawback of using protons over photons is the sensitivity of the former [1,2] to, e. g. anatomical changes, imperfect conversion between the Hounsfield Units and protons' stopping power [3–5], and setup errors [6]. These sources of error translate into uncertainties in the proton range. In lungs, this problem is magnified by continuous anatomical deformations due to breathing. Therefore, having real-time information about tumor position and its surrounding anatomy is of great value in treating lung cancer with proton therapy.

Techniques involving an external surrogate for instance placed on the skin of the patient, have been suggested to monitor tumor motion; however, the external surrogate may not be perfectly correlated with the actual tumor position. Some reports in literature demonstrate poor correlation between the external motion monitored by a surrogate and the tumor position. Average errors of >0.5 cm have been reported in [7], while errors ~ 0.5 cm were reported as the best case scenario in [8]. Other studies report even worse correlations [9]. To overcome this problem, internal surrogates are needed. In this note, we propose to use the Promt gamma camera (PGC) [10–14] as an internal surrogate of motion.

We investigate via simulations the correlations between the PG profiles of the respiratory phases (RP) and the timing sequence of pencil beam scanning (PBS) in the presence of two sources of error: PG detection noise and irregularities in the breathing frequency.

2. Methods

2.1. Virtual data acquisition

We began with a 4D-CT of a patient with lung cancer, a treatment plan and the delivery timing sequence of the pencil beams (PB), which

* Corresponding author.
E-mail address: jaroslav.albert@uclouvain.be (J. Albert).

https://doi.org/10.1016/j.ejmp.2019.06.006
Received 30 December 2018; Received in revised form 16 May 2019; Accepted 15 June 2019
Available online 21 June 2019
1120-1797/ © 2019 Associazione Italiana di Fisica Medica. Published by Elsevier Ltd. All rights reserved.

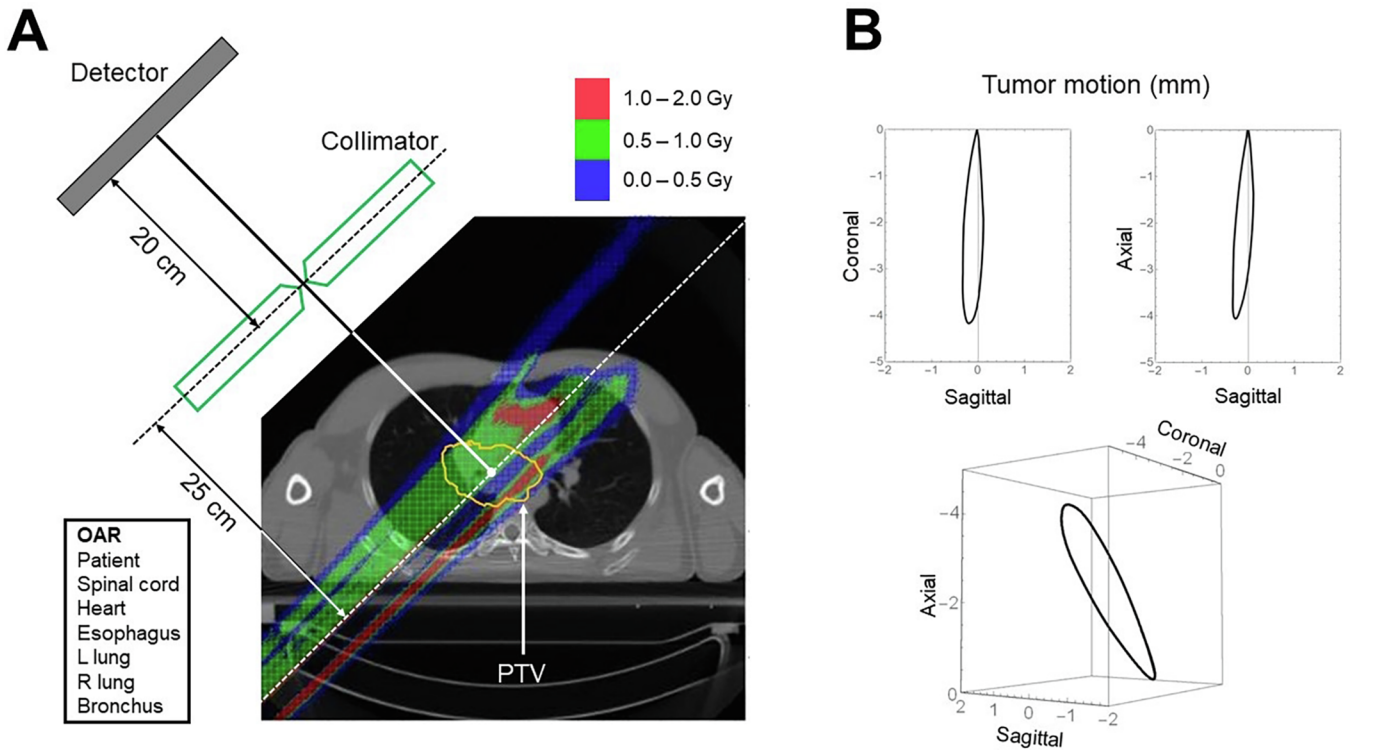

Fig. 1. A) Axial view of the CT at the first RP; dose from beam 1 computed on a CT averaged over the ten RPs; and the PGC set up. Also shown are the PTV contour and a list of organs at risk. B) Tumor motion over one period (four seconds).

was estimated using the ScanAlgo module of the IBA Proton Therapy System. The ScanAlgo is a tool that simulates an ideal irradiation with nominal timing. For the present treatment plan, the timing sequence stipulated by ScanAlgo was such that PBs for a specific energy, from now on referred to as layers, occurred within a few milliseconds, followed by a pause of 2 s (plus/minus a few milliseconds). The 4D-CT consisted of ten 3D-CTs, each corresponding to a different RP. The RPs were separated by 0.4 s, adding up to a breathing period of 4 s. Next, we used a morphon deformable registration algorithm [15] to interpolate the deformation field between two successive RPs, thus obtaining four intermediate values of the deformation field. The result was 50 CTs corresponding to 50 RPs separated by $\Delta t = 0.08$ s. The treatment plan was created on RayStation via a 2-field Intensity Modulated Proton Therapy optimization for research purposes only. For the purposes of this study, we chose to work only with beam 1, whose gantry angle was 225 degrees, and consisted of 147 PBs grouped into ten layers. Fig. 1 A) shows the dose on the average CT, the PTV contour, the PGC setup and the list of OARs. Fig. 1 B) shows the tumor motion over one period.

Next, we introduced breathing irregularities according to the following procedure. If the breathing was regular (no breathing irregularities), the timing between any two consecutive RPs would be constant, e. i. $\Delta t_0 = 0.08$ s. If, however, the breathing was irregular, this time difference would vary as a function of the RPs. If we let n be the integer that labels the RPs, then the relationship between real time and n can be written as:

$$\sum_{m=1}^{n} \Delta t(m) = t_n, \tag{1}$$

where t_n is the time corresponding to the n^{th} RP. We have chosen Δt to be:

$$\Delta t(n) = \Delta t_0 f(n), \tag{2}$$

where

$$f(n) = 1 + a_1 G(n, \mu_1, \sigma_1) + a_2 G(n, \mu_2, \sigma_2), \tag{3}$$

and $G(n, \mu, \sigma) = e^{-(n-\mu)^2/(2\sigma^2)}$. The range of a_1 and a_2, was set to $[-0.2, 0.2]$. The parameters μ_1 and μ_2 specify the times at which the errors occur; their range was $[0, 250]$. The parameters σ_1 and σ_2 give the average duration of the breathing irregularity in n-space and both have the range $[10, 50]$. When μ_1 and μ_2 are close to each other, one can think of $f(n)$ as representing a single, but more complex, breathing irregularity. With a larger number of Gs one could construct a more complex model of breathing irregularities; however, for the purposes of this paper, we have restrict this number to two.

The choice of the range for the μs and σs is related to the overall beam delivery time, which is about 20 s. The maximum for the μs, 250, which corresponds to 20 s ($250\Delta_0 = 20$). This ensures that the breathing irregularities occur by the end of the treatment. Similarly, we want the σs to be on the order of the treatment duration. Since a Gaussian distribution has a width that is about 6 times its standard deviation, the maximum σ of 50 gives a spread of 24 ($6 \times 50 \times \Delta_0 = 24$). The range for a_1 and a_2 was chosen such that the maximal and minimal deviation of $f(n)$ from 1 was 40% ($a_1 = a_2 = 0.2$) and -40% ($a_1 = a_2 = -0.2$), respectively.

We generated fifty parameter sets $(a_1, a_2, \mu_1, \mu_2, \sigma_1, \sigma_2)$ sampled from a square distribution according to the aforementioned range of each parameter. Also generated for each case was the start time of the treatment between $t = 0$ s and $t = 4$ s. As shown in Fig. 2, this simple model of breathing irregularities produces phase shifts in the breathing cycle that are consistent with observations of real patients [16–18].

The RPs corresponding to the 10 layers were then computed according to Eq. (2):

$$n_i = \min \left| \sum_{m=1}^{n_i} \Delta t(m) - t_i^{treat} \right|, \tag{4}$$

where n_i is the n^{th} RP through which the i^{th} pencil beam passes.

Finally, using an analytical simulation tool based on pre-computed Monte Carlo emission profiles [20], we simulated the PG profiles. This method has been validated by PG measurement studies [11–14]. This

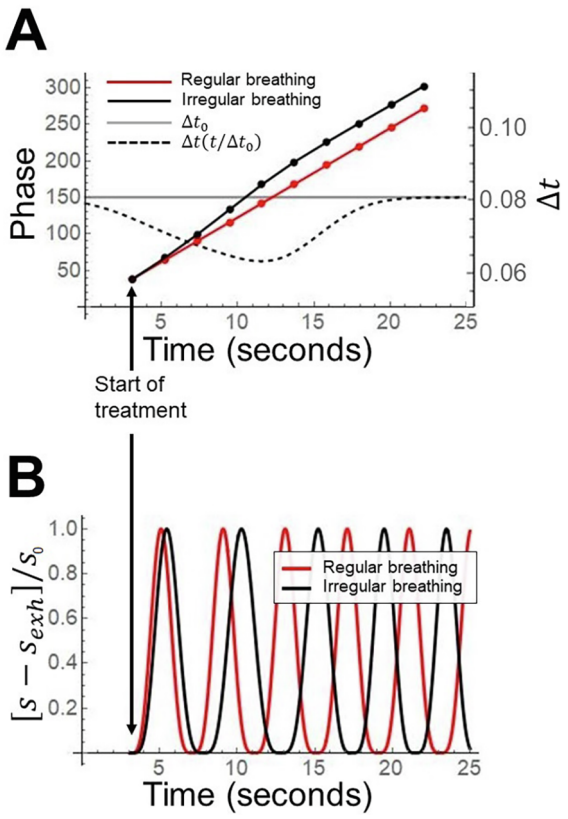

Fig. 2. Example of regular versus irregular breathing. A) Time versus RPs (left vertical axes) and Δt (right vertical axes). The dots represent the layers for regular breathing (red) and irregular breathing (black). The gray and the dashed lines show the time dependence of Δt for regular and irregular breathing, respectively. B) Example of tumor motion for the breathing irregularity in A. The red line represents regular breathing and is given by the formula $s(t) = s_{exh} - s_0 \sin^4(\pi t/T - \phi)$[19], where T is the period. The black line represents irregular breathing, given by the sum formula Eq. (1) but with t replaced by $\int_0^t f(x)dx$, which is merely the continuous version of Eq. (1). The variable s appearing on the vertical axes is the absolute value of the distance between the average and instantaneous center of mass of the tumor. s_0 is the amplitude and s_{exh} is s at exhalation. For convenience, the phase ϕ was chosen to be $\pi t_1/T$, where t_1 is the time of treatment initiation. (For interpretation of the references to colour in this figure legend, the reader is referred to the web version of this article.)

was repeated for every one of the 50 cases, where by "case" we mean a unique breathing irregularity and start time. In order to simulate a realistic PG signal, we added Poisson noise to all PG profiles, and repeated the procedure fifty times per case. Thus, for each unique setup and breathing irregularity, we generated fifty "sub-cases," adding up to 2500 cases in total. We will refer to these profiles as virtual, and label them PG^{virt}.

2.2. Simulated data acquisition

We simulated clean PG profiles (no setup errors or Poisson noise) for every pencil beam passing through all fifty RPs. To distinguish them from PG^{virt}, these profiles will be labeled as PG^{sim}. Fig. 3 shows eight examples of PG^{virt} (black dots) superimposed over the fifty PG^{sim} (gray curves) for the first layer, which contained eight pencil beams.

2.3. Estimating the respiratory phases from PG profiles

Since the pencil beams within each layer are separated by only a few milliseconds, they pass approximately through the same RP. Thus, one only needs to estimate the RPs for the 10 layers, not each individual pencil beam. To estimate these RPs, we minimize the score function

$$d_k(c) = \sum_{b=1}^{L(k)} \sum_{m=1}^{20} |PG^{virt}_{k,b,m} - PG^{sim}_{k,b,m}(c)|, \tag{5}$$

where k and b refer to layer and pencil beam (in that layer), respectively, while m labels the detector bins. The upper bound $L(k)$ is the number of pencil beams in layer k, and c labels the RPs.

The score function in Eq. (5) compares the virtual and simulated PG profiles within each layer independently of the other layers. Thus, to minimize Eq. (5) with respect to c for each layer k, one only needs to list the values of $d_k(c)$ for all $0 < c < 51$ and pick the c that corresponds to the smallest d_k. Another approach is to impose a parameter-dependent correlation between the layers. For example, if the breathing frequency was increased/decreased by a constant, the breathing would still be regular and hence the RPs of all the layers would fall on a straight line. In Fig. 4, we show a two-dimensional view of this approach. The white dashed line is a result of optimizing

$$S(\alpha_1, \alpha_0) = \sum_{k=1}^{10} d_k(\alpha_1 k + \alpha_0) \tag{6}$$

with respect to α_0 and α_1. Note that a linear correlation between the layers will lead to a good approximation only when the breathing irregularities are small. For larger errors, the correlation curve may be more complicated, e.g. a second order polynomial: $\alpha_2 k^2 + \alpha_1 k + \alpha_0$.

We have tested all three methods – independent, linear and quadratic – for all cases and sub-cases. For the independent estimation, we used the *Position* function in Mathematica to find the discrete value of c that minimized $d_k(c)$. For the other two methods, we used a direct random search to minimize $S(\vec{\alpha})$ with respect to $\vec{\alpha}$. The parameter set $\vec{\alpha}$ that yielded the lowest $S(\vec{\alpha})$ out of one hundred thousand samples, drawn from a square distribution, was chosen. For the linear case, the parameters α_0 and α_1 were constrained according to $\alpha_1 = m = [m_{min}, m_{max}]$, where m_{min} and m_{max} are the minimum and maximum slope, respectively, and $\alpha_0 + \alpha_1 = p$, where p is the initial phase. The slope is k-dependent: $m = 2\alpha_2 k + \alpha$. In order to satisfy the slope condition $m = [m_{min}, m_{max}]$, we must put constraints on α_0, α_1 and α_2 for two cases: $\alpha_2 > 0$, a down parabola; and $\alpha_2 < 0$, an up parabola. For parabolas that are monotonically increasing ($\alpha_2 > 0$) in the domain $k = [1, 10]$, the smallest slope is always at $k = 1$, while the largest slope is always at $k = 10$. The inequalities that satisfy these conditions read

$$\begin{aligned} 2\alpha_2 + \alpha_1 &\geqslant m_{min} \\ 20\alpha_2 + \alpha_1 &\leqslant m_{max}, \end{aligned} \tag{7}$$

and their solution is $0 \geqslant \alpha_2 \leqslant (m_{max} - m_{min})/18$ and $(m_{max} - 20\alpha_2) \geqslant \alpha_1 \geqslant (m_{min} - 2\alpha_2)$. The condition for α_0 is set by restricting the initial phase: $0 \leqslant \alpha_2 + \alpha_1 + \alpha_0 \leqslant p$. For the case $\alpha_2 < 0$ refer to Table 1, which shown all the parameter conditions for the linear and the quadratic model for $m_{min} = 20$, $m_{max} = 30$ and $p = [1, 50]$.

To estimate the quality of our models, we define an average estimation error ΔRP:

$$\langle \Delta RP \rangle = \frac{1}{M} \sum_{k=1}^{M} |\Delta RP_k|, \tag{8}$$

which gives the minimal distance between the estimated RP and the virtual RP. For example, if the virtual RP was 46 and the estimated RP was 1, then the absolute value of the error would be $51 - 46 = 5$ (or 0.4 s), since RP 1 is the same RP as 51. However, a more clinically relevant quantity is the dose. Thus, we also define

$$\Delta_k(t, i) = D_k(0, \mathbf{x}_i) - D_k(t, \mathbf{x}_i + \delta \mathbf{x}_i), \tag{9}$$

where $D_k(0, \mathbf{x}_i)$ is the dose in Gy delivered to voxel i, whose coordinates are $\mathbf{x}_i$, at the RP $k = 1, \ldots, 10$ and at the time $t = 0$; and $D(t, \mathbf{x}_i + \delta \mathbf{x})$ is the dose at the same voxel i that has migrated to the new coordinate

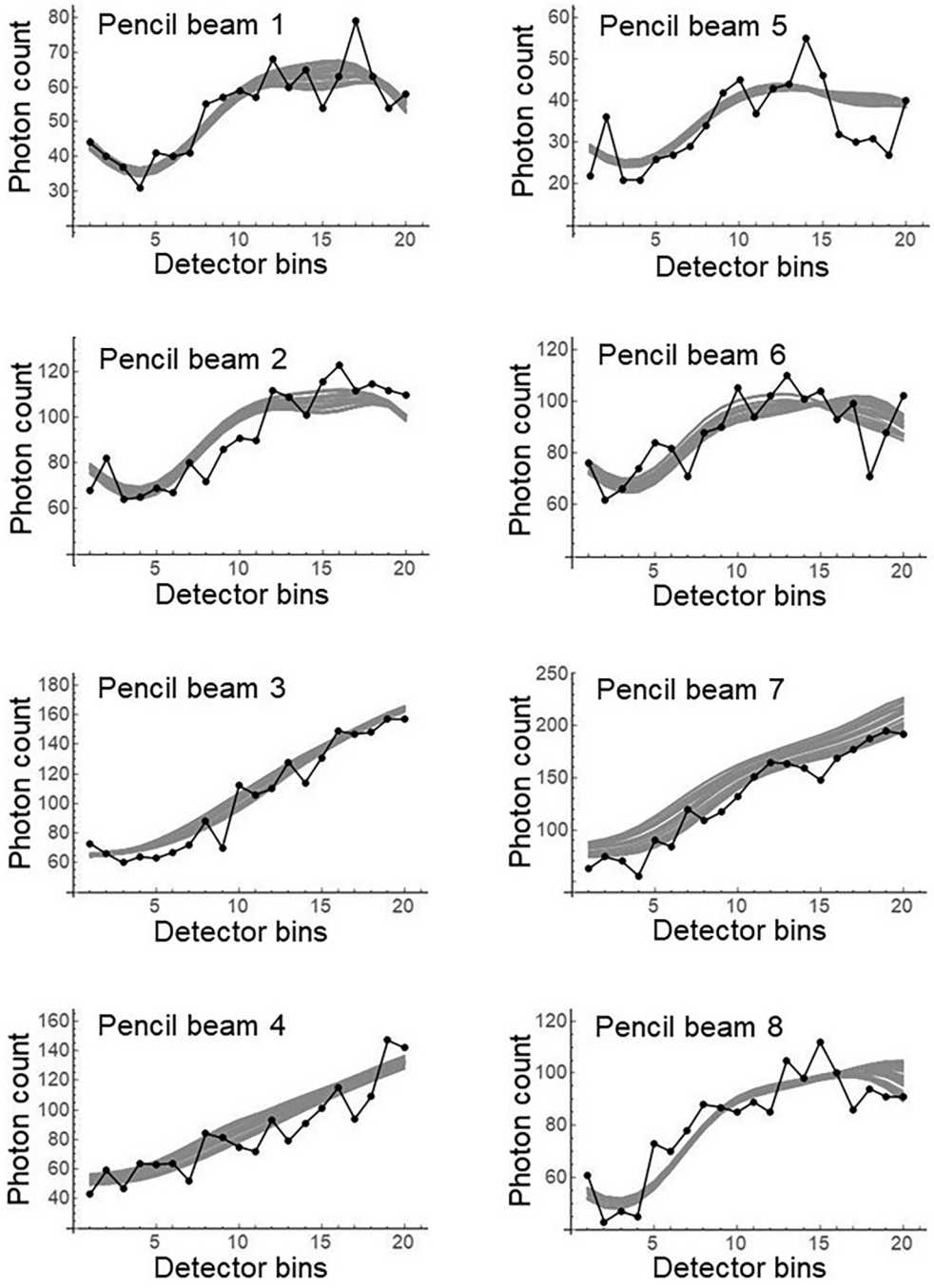

Fig. 3. Example of PG profiles of pencil beams in the first layer. The black dots represent the PG^{virt}. The gray curves are the PG^{sim} for a same pencil beam passing through the fifty RPs.

$\mathbf{x}_i + \delta\mathbf{x}_i$ within the time t. Then, we compute the average

$$\mu_k(t) = \frac{1}{N_V}\sum_{i=1}^{N_V} \Delta_k(t, i), \tag{10}$$

and standard deviation

$$\sigma_k(t) = \left[\frac{1}{N_V}\sum_{i=1}^{N_V} [\Delta_k(t, i) - \mu_k(t)]^2\right]^{1/2}, \tag{11}$$

where the summation index i runs over N_V voxels of the PTV. To estimate the error in dose we are making by employing our method, we compute the relative average $\mu_r(t) = \mu_k(t)/\langle D_k\rangle$ and relative standard deviation $\sigma_r(t) = \sigma_k(t)/\langle D_k\rangle$, where $\langle D_k\rangle$ is the average dose at RP k at $t = 0$:

$$\langle D_k\rangle = \left[\frac{1}{N_V}\sum_{i=1}^{N_V} D_k(0, \mathbf{x}_i)\right]. \tag{12}$$

3. Results

Fig. 5A, B and C show the results yielded by the three models in terms of an average estimation error, ΔRP (left), and by the average and standard deviation of the estimation error for each layer (right). The

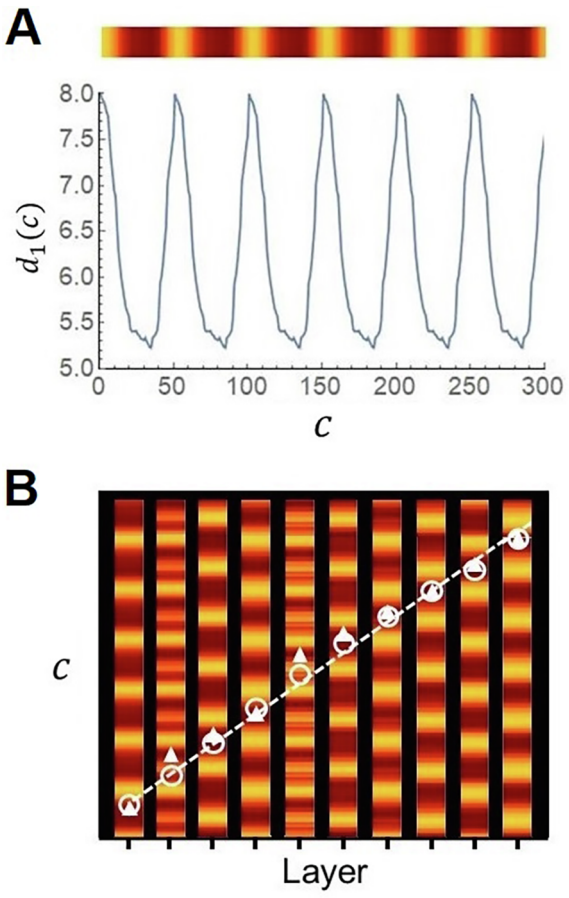

Fig. 4. A) Example of phase, c, versus $d_k(c)$ for layer 1. B) A density plot for $d_1(c)$ through $d_{10}(c)$ as a function of layers and phases. The center of the white circle indicates the correct phase for each layer, k. The white triangles, referring to the independent method; their centers coincide with the local minima, i.e. the estimated phase for each k. The white line is the best linear fit stipulated by the minimum of Eq. (6).

bottom axes of Fig. 5 A, B and C gives the time in seconds, while the top axes indicates tumor displacement in millimeters assuming the initial RP was 5. We chose this initial RP because the tumor position has the largest velocity near this phase. Thus, this choice corresponds to the worst case, i. e. the largest possible deviation within the 90% confidence interval. For the first layer only, we also computed μ_r and σ_r for $k = 1, 5, 7$ for $t = \Delta t_0 n = 0.08n$ (see section "Virtual data acquisition"), where $n = 1, ..., 50$; the points were then interpolated. Although the relative average dose deviation (black curve) is negligible, the relative standard deviation (gray curve) can be as large as 150% of the initial average dose. Also shown in Fig. 5 D) are the 90% confidence intervals for the three models. For the independent model (gray disk), the 90% mark of the confidence interval gives σ_r relative to the maximum σ_r of 13% for $k = 1$, 19% for $k = 5$ and 15% for $k = 7$. In the same order, the σ_rs relative to the maxima are 24%, 27% and 33% for the linear model (open circle), while for the quadratic model (black disk) they are 11%, 17% and 12%.

3.1. Discussion

We have implemented a proof-of-concept which confirms that, in the presence of detection noise and irregularities in the breathing frequency, PGC can be used to estimate RPs with model-dependent degrees of accuracy. Of the three models considered – independent, linear and quadratic – the quadratic model was the most accurate, with an uncertainty of <5% of the breathing period with 90% confidence, but somewhat less reliable than the independent model, due to more prevalent outliers. On a layer-to-layer basis, the averages of the independent and the quadratic models are very similar; however, the former has smaller standard deviation in layers 3 and 4. The linear model is the least accurate of all, both on average and on layer-to-layer basis. In terms of dose reconstruction for layer 1, the independent and the quadratic models predict the phase with an accuracy that, for the starting phase 5, translates into a dose uncertainty of 19 and 17%, respectively, relative to the maximum dose uncertainty. Although less accurate on average than the quadratic model, the advantage of the independent model is that it is not affected by sudden changes in breathing; whereas the quality of the linear and the quadratic models relies on relatively smooth breathing irregularities.

All the computations leading to our results were done on a planning 4D-CT. In order for our methodology to be applicable for any fraction, it is required that one has a daily 4D-CT for each fraction, on which the PG profiles can be computed. However, obtaining a daily 4D-CT exposes the patient to a significant amount of radiation over the entire treatment. An alternative would be to use a 4D-CBCT reconstruction algorithm [21,22] that uses projections acquired for the 3D-CBCT used inside the treatment room to align the patient. This way, one can obtain a 4D-CBCT for the same price (in terms of the dose) as the 3D-CBCT that is acquired for the patient alignment. In order to compute the Prompt gamma profiles from the 4D-CBCT, one could use a methodology reported in [23] to compute a virtual CT using the planning 4D-CT and the reconstructed 4D-CBCT. The next step for our methodology would be to repeat all the computations performed herein on virtual CTs reconstructed via the methods in [21,23].

One possible application of the methods presented herein could be to detect interfractional anatomical changes. Observing a failure of the correlation between the RPs estimated by an external surrogate and those estimated via the present method (internal surrogate) would indicate a deformation in the anatomy. Although the PGC is not sensitive enough to reveal the nature of the deformation, a large enough mismatch between the two techniques would be a bases for stopping the treatment. Another variation of this approach would be to employ the proposed internal surrogate for treatments involving mechanical breathing [24]. In such a setting, the breathing irregularities would be dramatically reduced, which would increase the accuracy of the proposed internal surrogate, thus making it more sensitive to finer anatomical changes.

In order to evaluate the proposed techniques, more work will be needed to test the PGC as a RP estimator, e. g. against irregularities in the breathing amplitude and patients setup errors.

Table 1
Parameter ranges for the linear and the quadratic model for $m = [20, 30]$ and $p = [0, 50]$.

Parameter	Linear	Quadratic ($\alpha_2 < 0$)	Quadratic ($\alpha_2 > 0$)
α_2	0	$[-5/9,0)$	$(0,5/9]$
α_1	[20,30]	$[20 - 20\alpha_2, 30 - 2\alpha_2]$	$[20 - 2\alpha_2, 30 - 20\alpha_2]$
α_0	$[\alpha_1 + 1, 50 + \alpha_1]$	$[1 - \alpha_2 - \alpha_1, 50 - \alpha_2 - \alpha_1]$	$[1 - \alpha_2 - \alpha_1, 50 - \alpha_2 - \alpha_1]$

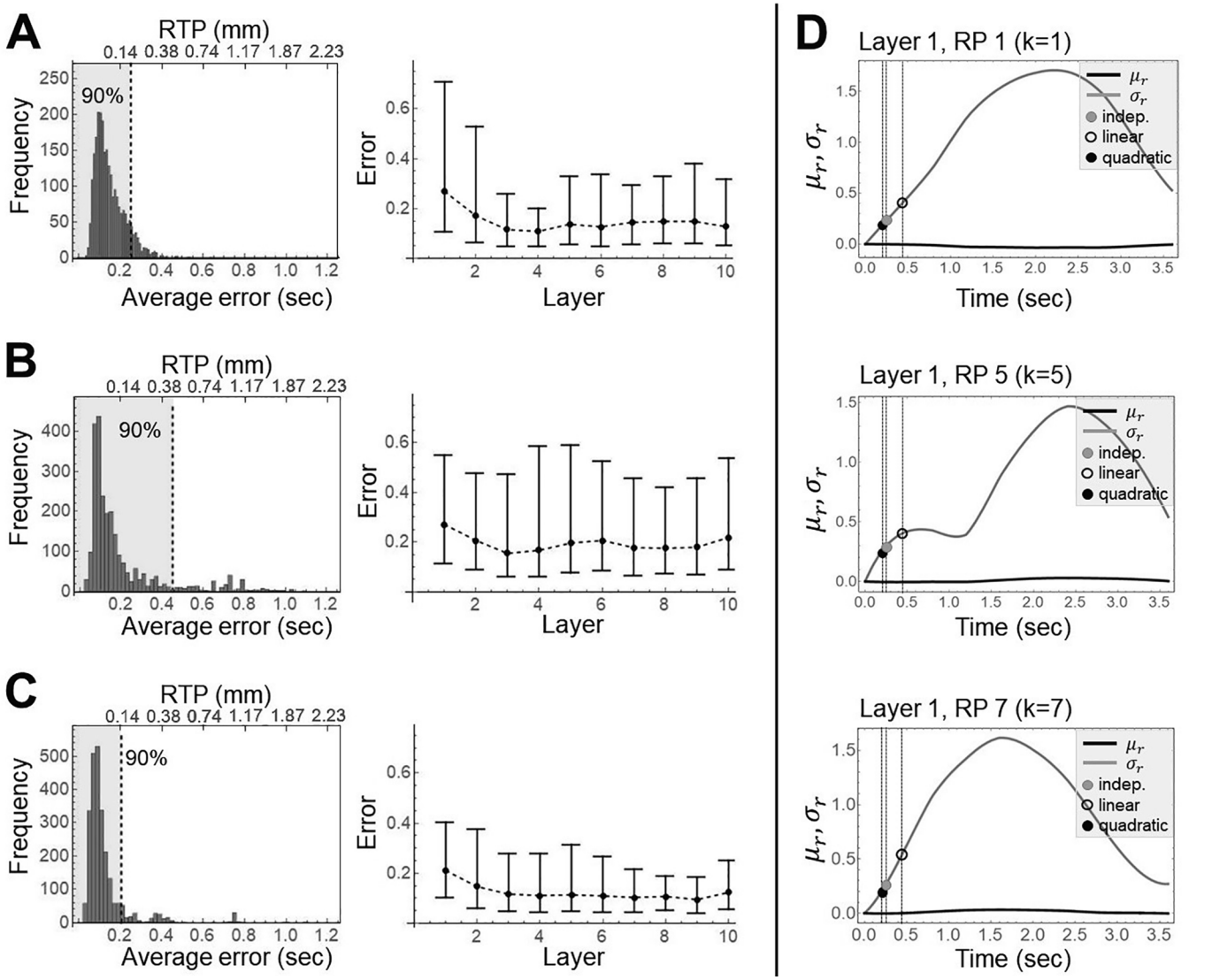

Fig. 5. Distribution of $\langle \Delta RP \rangle$ for the independent A, the linear B, and the quadratic method C. The vertical dashed lines in the histograms on the left indicate the 90th percentile mark. The bottom axes indicates time in seconds, while the top axes shows the relative tumor position (RTP) with respect to RP 5. The plots on the right show the average and the standard deviation of the estimation error in seconds for each layer. D) μ_r, and σ_r for the first layer at $k = 1, 5, 7$ as defined in Eqs. (10), (11), (9).

Acknowledgments

This research project was made possible by ImagX-R research program. JA would like to thank E. Ejkova for her technical support.

References

[1] Paganetti H. Range uncertainties in proton therapy and the role of Monte Carlo simulations. Phys Med Biol 2012;57(11):R99–117.
[2] Engelsman M, Schwarz M, Dong L. Physics controversies in proton therapy. Semin Radiat Oncol 2013;23(2):88–96.
[3] Schneider U, Pedroni E, Lomax A. The calibration of CT Hounsfield units for radiotherapy treatment planning. Phys Med Biol 1996;41:111–24.
[4] Besemer A, Paganetti H, Bednarz B. The clinical impact of uncertainties in the mean excitation energy of human tissues during proton therapy. Phys Med Biol 2013;58(4):887–902.
[5] Yang M, Zhu XR, Park PC, Titt U, Mohan R, Virshup G, et al. Comprehensive analysis of proton range uncertainties related to patient stopping-power-ratio estimation using the stoichiometric calibration. Phys Med Biol 2012;57:4095–115.
[6] van Herk M, Remeijer P, Rasch C, Lebesque J. The probability of correct target dosage: dose-population histograms for deriving treatment margin in radiotherapy. Int J Radiat Oncol Biol Phys 2000;47(4):1121–35.
[7] Malinowski KT, McAvoy TJ, George R, Dieterich S, DSouza WD. Mitigating errors in external respiratory surrogate-based models of tumor position. Int J Radiat Oncol Biol Phys 2012;82(5):e709–16.
[8] Wölfelschneider J, Brandt T, Lettmaier S, Fietkau R, Bert C. Quantification of an external motion surrogate for quality assurance in lung cancer radiation therapy. Biomed Res Int 2014;2014:595430.
[9] Zhang F, Kelsey C, Yin F, Cai J. Correlation between external surrogate motion and lung tumor motion: from a statistical point of view. Radiat Oncol 2014;81(2):781–2.
[10] Priegnitz M, Barczyk S, Nenoff L, Golnik C, Keitz I, Werner T, et al. Towards clinical application: prompt gamma imaging of passively scattered proton fields with a knife-edge slit camera. Phys Med Biol 2016;61(22).
[11] Xie Y, Bentefour EH, Janssens G, Smeets J, Vander Stappen F, Hotoiu L, et al. Prompt gamma imaging for in vivo range verification of pencil beam scanning proton therapy. Int J Radiat Oncol Biol Phys 2017;99(1):210–8.
[12] Janssens G, Smeets J, Vander Stappen F, Prieels D, Clementel E, Hotoiu EL, et al. Sensitivity study of prompt gamma imaging of scanned beam proton therapy in heterogeneous anatomies. Radiother Oncol 2015:1–6.
[13] Priegnitz M, Helmbrecht S, Janssens G, Perali I, Smeets J, Vander Stappen F, et al. Detection of mixed-range proton pencil beams with a prompt gamma slit camera. Phys Med Biol 2015;60(12):4849–71.
[14] Nenoff L, Priegnitz M, Janssens G, Petzoldt J, Wohlfahrt P, Trezza A, et al. Sensitivity of a prompt-gamma slit-camera to detect range shifts for proton treatment verification. Radiother Oncol 2017:21–3.
[15] Plumat J, Andersson MG, Janssens G, Orban de Xivry J, Knutsson H. Image registration using the Morphon algorithm: an ITK implementation; 2009.
[16] Nishioka S, Nishioka T, Kawahara M, Tanaka S, Hiromura T, Tomita K, et al. Exhale fluctuation in respiratory-gated radiotherapy of the lung: a pitfall of respiratory gating shown in a synchronized internal/external marker recording study. Radiother Oncol 2008;86(1):69–76.
[17] Pepin EW, Wu H, Shirato H. Dynamic gating window for compensation of baseline

shift in respiratory-gated radiation therapy. Med Phys 2011;38(4):1912–8.
[18] Gendrin C, Furtado H, Weber C, Bloch C, Figl M, Pawiro SA, et al. Monitoring tumor motion by real time 2D/3D registration during radiotherapy. Radiother Oncol 2011;102(2):274–80.
[19] Seppenwoolde Y, Shirato H, Kitamura K, Shimizu S, van Herk M, Lebesque JV, et al. Precise and real-time measurement of 3D tumor motion in lung due to breathing and heartbeat, measured during radiotherapy. Int J Radiat Oncol Biol Phys 2002;53(4):822–34.
[20] Janssens G, Smeets J, Vander Stappen F, Prieels D, Priegnitz M, Perali I, et al. Analytical computation of prompt gamma ray emission and detection for proton range verification. Phys Med Biol 2015;60(12):4915–46.
[21] Mory C, Janssens G, Rit S S. Analytical computation of prompt gamma ray emission and detection for proton range verification. Phys Med Biol 2016;61(18):6856.
[22] Niepel K, Kamp F, Kurz C, Hansen D, Rit S, Neppl S, et al. Feasibility of 4DCBCT-based proton dose calculation: an ex vivo porcine lung phantom study. Z Med Phys 2018;10771.
[23] Veiga C, Janssens G, Teng C-L, Baudier T, Hotoiu L, McClelland JR, et al. First clinical investigation of cone beam computed tomography and deformable registration for adaptive proton therapy for lung cancer. Int J Radiat Oncol* Biol* Phys 2016;95(1):549–59.
[24] Van Ooteghem G, Dasnoy-Sumell D, Lemaire G, Liistro G, Sterpin E, Geets X. Mechanically-assisted and non-invasive ventilation: Innovative step forward in the motion management; 2018.https://doi.org/10.1016/S0167-8140(18)30722-9.